Excitons in strain-induced one-dimensional moiré potentials at transition metal dichalcogenide heterojunctions

Yusong Bai [1,7], Lin Zhou [1,2,7], Jue Wang [1], Wenjing Wu [1], Leo J. McGilly [3], Dorri Halbertal [3], Chiu Fan Bowen Lo [3], Fang Liu [1], Jenny Ardelean [4], Pasqual Rivera [5], Nathan R. Finney [4], Xu-Chen Yang [6], D. N. Basov [3], Wang Yao [6], Xiaodong Xu [5], James Hone [4], Abhay N. Pasupathy [3 ✉] and X.-Y. Zhu [1 ✉]

The possibility of confining interlayer excitons in interfacial moiré patterns has recently gained attention as a strategy to form ordered arrays of zero-dimensional quantum emitters and topological superlattices in transition metal dichalcogenide heterostructures. Strain is expected to play an important role in the modulation of the moiré potential landscape, tuning the array of quantum dot-like zero-dimensional traps into parallel stripes of one-dimensional quantum wires. Here, we present real-space imaging of unstrained zero-dimensional and strain-induced one-dimensional moiré patterns along with photoluminescence measurements of the corresponding excitonic emission from WSe$_2$/MoSe$_2$ heterobilayers. Whereas excitons in zero-dimensional moiré traps display quantum emitter-like sharp photoluminescence peaks with circular polarization, the photoluminescence emission from excitons in one-dimensional moiré potentials shows linear polarization and two orders of magnitude higher intensity. These results establish strain engineering as an effective method to tailor moiré potentials and their optoelectronic response on demand.

The formation of interfacial moiré patterns through angular and/or lattice mismatch has become a powerful approach to engineering a range of quantum phenomena in van der Waals heterostructures[1–4]. For long-lived and valley-polarized interlayer excitons in transition metal dichalcogenide (TMDC) heterobilayers[5], signatures of quantum confinement derived from the moiré landscape have been reported in recent experimental studies[6–10]. Such moiré confinement has offered the exciting possibility to tailor new excitonic systems, such as ordered arrays of zero-dimensional (0D) quantum emitters in topological superlattices[1,11]. The two-dimensional (2D) nature of the material system dictates that the moiré potential can be strongly influenced by strain; a small uniaxial strain can tune the array of quantum dot-like 0D traps into parallel stripes of one-dimensional (1D) quantum wires[4]. In this work, we directly imaged 0D and 1D moiré potentials and determined the corresponding excitons from photoluminescence (PL) emission from WSe$_2$/MoSe$_2$ heterobilayers. We chose the WSe$_2$/MoSe$_2$ heterobilayer as a model system because moiré interlayer excitons trapped in moiré potentials have recently been reported for this heterobilayer system[6,7].

0D versus 1D moiré patterns and PL spectra
The heterobilayer was obtained by the transfer stacking method[12,13], either sandwiched between thin hexagonal boron nitride (h-BN) flakes (Fig. 1a) or on a h-BN flake but with no top h-BN capping layer. TMDC heterobilayers are intrinsically endowed with moiré landscapes, as illustrated by the hexagonal moiré pattern in Fig. 1b with period $b \approx a/\sqrt{(\Delta\theta)^2 + \delta^2}$, where a is the monolayer lattice constant, δ is the lattice mismatch and $\Delta\theta$ is the twist angle[1,14]. The

twist angle can be determined by second harmonic generation (SHG) measurements[15]. This moiré pattern can be strongly modified by applying differential strain (that is, inequivalent strains on the two constituting layers). Specifically, a modest uniaxial strain can transform the moiré pattern into a hierarchy consisting of a primary structure of elongated ovals (arrows) that lie parallel to each other to form a secondary structure of pseudo-1D stripes (dashed lines, Fig. 1c). Under differential and uniaxial tensile strain, the elongated ovals merge into 1D stripes for sufficiently small $\Delta\theta$ (from 0° or 60°) (Fig. 1d)[4].

As we establish below, the 0D and 1D moiré patterns give rise to two distinctive types of PL spectra at low excitation densities ($n_{ex} \leq 1 \times 10^{11}$ cm^{-2}). For ~20% of samples, we observe sharp PL peaks with the full-width at half-maximum (FWHM) ≤ 1 meV. This type-I emission features strong circular polarization under circularly polarized excitation (Fig. 1e, upper), in agreement with a recent report[6]. For the majority of samples (~80%), we observe a single broad PL peak with FWHM $= 8 \pm 2$ meV, labelled as type-II emission (Fig. 1e, lower), in agreement with all other previous reports on interlayer excitons in the WSe$_2$/MoSe$_2$ heterobilayer[13,16,17]. We find that in contrast to type-I PL emission, there is little circular but strong linear polarization in type-II emission. For either AA- ($\Delta\theta$ close to 0°) or AB-stacked ($\Delta\theta$ close to 60°) samples, the type-II PL intensity is over two orders of magnitude higher than that of type-I.

Piezoresponse force microscopy imaging of 0D/1D moiré patterns
To establish the origins of the two types of PL features, we directly imaged the moiré superlattice structure using piezoresponse force

[1]Department of Chemistry, Columbia University, New York, NY, USA. [2]College of Engineering and Applied Sciences, Nanjing University, Nanjing, China. [3]Department of Physics, Columbia University, New York, NY, USA. [4]Department of Mechanical Engineering, Columbia University, New York, NY, USA. [5]Department of Physics and Department of Materials Science and Engineering, University of Washington, Seattle, WA, USA. [6]Department of Physics, University of Hong Kong, Hong Kong, China. [7]These authors contributed equally: Yusong Bai, Lin Zhou. ✉e-mail: apn2108@columbia.edu; xyzhu@columbia.edu
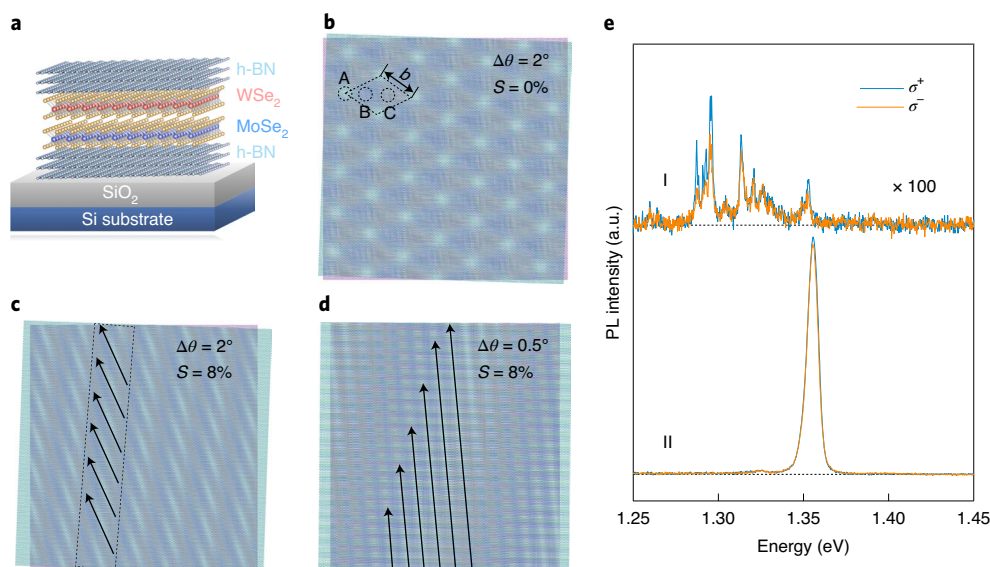
Fig. 1 | Hexagonal vs quasi-1D moiré patterns and the associated PL spectra. a, Schematic of the vertically stacked WSe_2/$MoSe_2$ heterobilayer with h-BN encapsulation on a SiO_2/Si substrate. **b,** Schematic of the hexagonal moiré superlattice with the supercell indicated by dashed lines. The moiré period is given by the expression $b \approx a/\sqrt{(\Delta\theta)^2 + \delta^2}$. A, B and C are high-symmetry points that preserve C_3 symmetry within each moiré unit cell. **c,d,** Quasi-1D (strained) moiré superlattices formed with a uniaxial strain (S) of 8% and twist angle ($\Delta\theta$) of 2 (**c**) and 0.5° (**d**). The arrows highlight the primary and the dashed rectangles the secondary 1D moiré structures. The quasi-1D moiré superlattices in **c** and **d** were formed with a uniaxial tensile strain of 8% on one (WSe_2) of the two monolayers. **e,** Representative PL spectra from two WSe_2/$MoSe_2$ heterobilayer samples with h-BN encapsulation showing type-I (upper) and type-II emission (lower). The dashed lines mark zero PL intensity. The blue and orange spectra represent right (σ^+) and left (σ^-) circularly polarized emission under σ^+ excitation, respectively. The PL spectra were obtained with excitation density $n_{ex} \approx 6.1 \times 10^9\,cm^{-2}$ at 4 K ($h\nu = 1.65\,eV$, repetition rate 76 MHz and pulse duration ~150 fs for all PL measurements).

microscopy (PFM). TMDC mono- and bilayers exhibit strong piezoelectric responses[18,19]. The moiré landscape in the heterobilayer modulates the piezoelectric tensor elements, leading to lateral deformations of the TMDC heterostructure in the presence of a vertically applied a.c. electric field. This electromechanical coupling is the basis for real-space imaging by PFM of the moiré patterns typically not visible in conventional atomic force microscopy (AFM)[20]. The h-BN/WSe_2/$MoSe_2$ stack, without the top h-BN capping layer, was first positioned on the soft polymer transfer tape (Fig. 2a) before transferring to the hard Si/SiO_2 substrate (Fig. 2b). We selected five locations for analysis (white areas labelled 1–5 in the AFM image, Fig. 2c). The PFM imaging of these areas on the soft polymer substrate reveals hexagonal moiré patterns, as shown in Fig. 2d–f, corresponding to spots 1–3. Additional PFM images of the hexagonal moiré patterns of spots 4 and 5 on this sample and other samples are shown in Supplementary Figs. 2b,d and 3a, respectively. Fast Fourier transforms (FFTs, bottom right insets) of the images in Fig. 2d–f identify six-fold symmetry, revealing superlattice constant $b = 17.0 \pm 1.7\,nm$, corresponding to $\Delta\theta = 58.9 \pm 0.1°$, in good agreement with the AB stacking of $\Delta\theta = 59.4 \pm 0.8°$ determined in the SHG measurements (Supplementary Fig. 1a).

After transferring the h-BN/WSe_2/$MoSe_2$ stack from the polymer tape to the Si/SiO_2 substrate, we carried out PFM imaging on exactly the same locations as before the transfer. Although some of the locations (1 and 4) retain the hexagonal moiré pattern, as shown in Fig. 2g and Supplementary Fig. 2e, other spots (2, 3 and 5) are transformed into distorted 1D moiré superlattices (Fig. 2h,i and Supplementary Figs. 2c and 3b). These 1D moiré patterns are consistent with the presence of uniaxial and differential strain, as illustrated in Fig. 1c,d. From extensive PFM imaging of multiple samples, we estimate that ~20% of the locations retain their original hexagonal 0D moiré pattern and ~80% are transformed from 0D to 1D moiré patterns. In Fig. 2h, the formation of large 1D stripes

with a longitudinal periodicity of $49.0 \pm 22.0\,nm$ is confirmed by the two-fold symmetry in the FFT (inset). In Fig. 2i, PFM imaging resolves the hierarchical 1D moiré patterns consisting of elongated ovals that lie parallel to each other (periodicity $9.3 \pm 0.6\,nm$) to form a secondary structure of 1D stripes (periodicity $25.6 \pm 5.6\,nm$).

To establish how differential strain is responsible for the transformation of the 0D hexagonal moiré patterns into the 1D moiré superlattices, we analysed the strain distribution using a continuum mechanics model, as detailed in Supplementary Text 1 and Supplementary Figs. 19–21. We chose Fig. 2i with a well-resolved hierarchical 1D moiré pattern to analyse the strain field. Figure 2j plots the grid representation of the extended PFM image in Fig. 2i, showing the strained moiré superlattice. The resulting magnitudes of the normal strain tensor elements $\tilde{\varepsilon}_{xx}$ and $\tilde{\varepsilon}_{yy}$ along the x and y directions are shown in Fig. 2k,l, respectively. As expected, the two strain fields are complementary to each other. The strain maps confirm the anisotropic nature of the strain field, which propagates in a direction ~30° from the x axis (see Supplementary Text 1 for details). The peak strain is $\pm 1.4\%$ for this particular 1D moiré pattern.

Linear PL polarizations from 1D moiré potentials

We analysed the excitonic properties derived from these distinct moiré patterns. The type-I PL shown in Fig. 1e is consistent with the spectral features reported before[6], and has been attributed to 0D moiré excitons in the hexagonal moiré landscape (Fig. 1b). In such a moiré landscape, the excitonic potential traps in each superlattice unit cell are located at high-symmetry points with C_3 symmetry[14,21], a prerequisite for preserving the valley optical selection rule and circularly polarized PL. At an excitation density of $n_{ex} \approx 1 \times 10^{10}\,cm^{-2}$, we estimate that the total number of interlayer excitons (N_{ex}) in a diffraction-limited focal spot (~$5 \times 10^{-8}\,cm^2$) is about 500. This finite number of excitons can be loaded into a finite number of quantum dot-like traps, with local variations due to heterogeneity
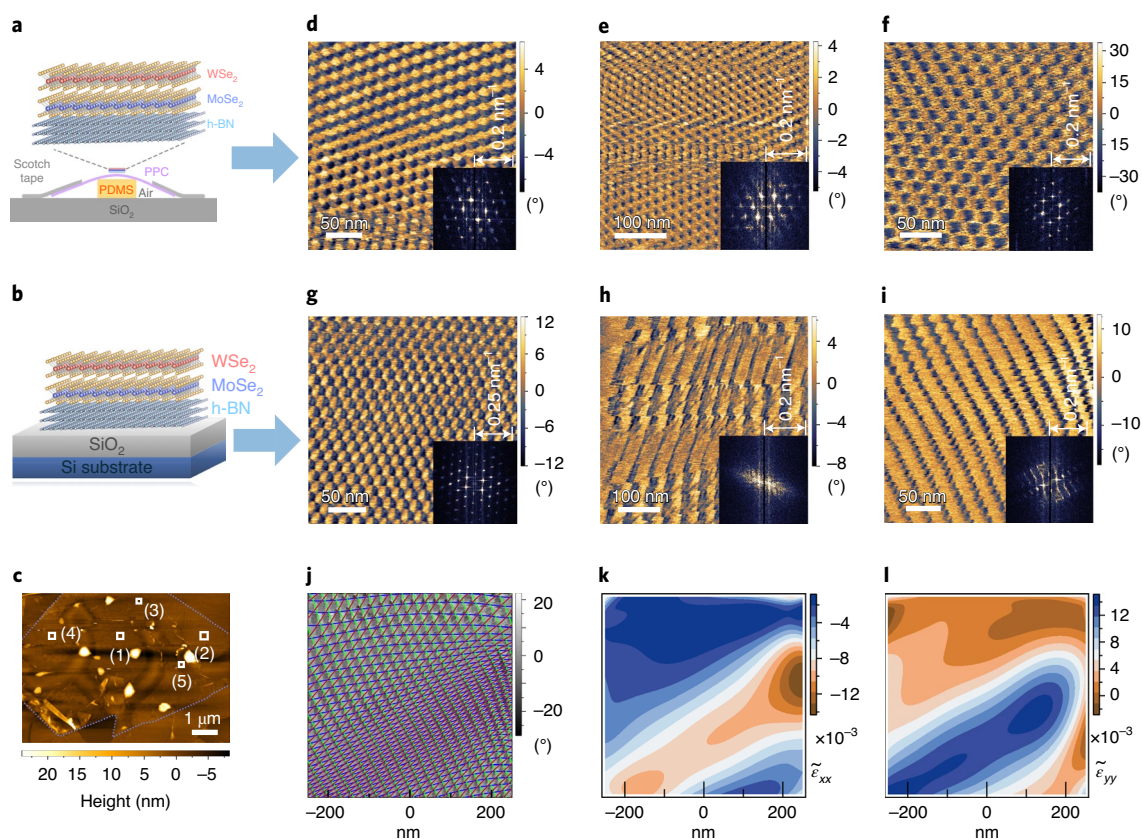
Fig. 2 | Transformation of moiré patterns and strain analysis. a,b, Schematics of the h-BN/WSe$_2$/MoSe$_2$ stack, without the top h-BN capping layer and with $\Delta\theta = 59.4 \pm 0.8°$, on air-cushioned polypropylene carbonate (PPC) tape (**a**) and the Si/SiO$_2$ surface (**b**). The air-cushion in **a** was generated by placing the PPC tape on top of a polydimethylsiloxane (PDMS) block and fixing the PPC to the SiO$_2$ surface at the perimeters with Scotch tape. **c,** AFM image of the WSe$_2$/MoSe$_2$ sample. The dashed lines mark the perimeter of the heterobilayer region and the white areas (labelled 1–5) are the spots imaged by PFM before and after transfer from PPC to Si/SiO$_2$. **d–i,** PFM images at three locations (corresponding to spots 1–3 in **c**) before (**d–f**) and after (**g–i**) transfer of the stack from the PPC tape to the Si/SiO$_2$ substrate. Insets: FFTs of the PFM images. **j–l,** Strain field analysis based on a continuum mechanics model for an extended region of the PFM image shown in **i**: 2D grid pattern (**j**) obtained from the PFM image and strain tensor element maps along the x axis ($\tilde{\varepsilon}_{xx}$, **k**) and y axis ($\tilde{\varepsilon}_{yy}$, **l**). Note that PFM and AFM are different imaging modes of the same microscope and the locations for PFM imaging were precisely determined from the AFM image.

in strain and electrostatics. As a result, one observes quantum dot-like PL peaks. We characterized in detail such type-I PL emission from a WSe$_2$/MoSe$_2$ heterobilayer sample with h-BN encapsulation (top and bottom) with a twist angle $\Delta\theta = 58.4 \pm 0.4°$ and sub-nanometre-scale flatness (Supplementary Fig. 4). The observation of sharp PL peaks with circular polarization is in excellent agreement with the recent report[6].

Note that the relatively thick h-BN capping layer (~20 nm) provides good electrostatic isolation of the WSe2/MoSe$_2$ heterobilayer, enabling the observation of sharp peaks in type-I PL emission, but it prohibits PFM imaging of the moiré patterns underneath. We fabricated another WSe$_2$/MoSe$_2$ heterobilayer with a thin (~2 nm) top h-BN encapsulation layer on a SiO$_2$/Si substrate (Supplementary Fig. 5a). The PFM image through the top h-BN cap reveals the hexagonal moiré pattern of the WSe$_2$/MoSe$_2$ heterobilayer (Supplementary Fig. 5b) with a superlattice constant of ~5.6 nm, corresponding to a twist angle of $\Delta\theta \approx 3.4°$. The PL spectrum recorded at the same spot as the PFM image shows partially resolved, sharp type-I emission with circularly polarized emission under σ^+ excitation (Supplementary Fig. 5c).

The type-II PL with a single emission peak, seen in ~80% of the samples with AA or AB stacking on Si/SiO$_2$ substrates, originates from the primary structure in the 1D moiré pattern. We correlated PFM imaging with PL polarization for five representative spots

(Fig. 2h,i and Supplementary Figs. 2c and 6b,c) from two different samples. Figure 3a–e shows the PL from these five spots with identified 1D moiré patterns. The corresponding polar plots of PL intensity versus linearly polarized detection angle in Fig. 3f–j show that all the peaks are linearly polarized. The direction of the linear polarization in each case (arrows in Fig. 3k–o) is aligned with the direction of one of the primary structures (golden fans in Fig. 3k–o) obtained from 2D-FFT analysis (Supplementary Fig. 7), but not with the direction of secondary 1D moiré structures (green fans in Fig. 3k–o).

Note that in Fig. 3k (from the PFM image in Fig. 2h), only the direction of the primary 1D moiré structure is resolved. In Fig. 3l,m (from the PFM images in Fig. 2i and Supplementary Fig. 2c, respectively), the 2D-FFT image analysis gives two to three apparent directions (golden fans), but only one of them represents the real direction of the primary 1D structure that aligns with the linear PL polarization direction. In Fig. 3n,o (from the PFM images in Supplementary Fig. 6b,c), the directions of the primary 1D structures are not clearly resolved from those of the secondary moiré structures.

We analysed the type-II PL emission in detail using a WSe$_2$/MoSe$_2$ heterobilayer sample sandwiched between h-BN (Supplementary Fig. 8), which is known to reduce electrostatic heterogeneity, decrease PL peak width and increase PL intensity[22].
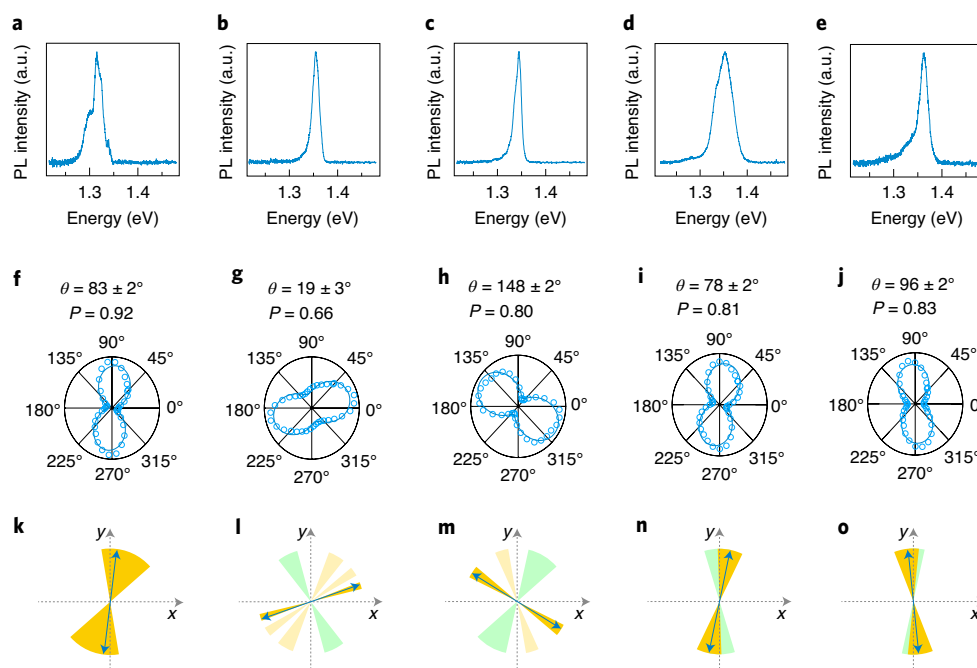
Fig. 3 | Direct correlation between 1D moiré patterns and linearly polarized PL emission. a–e, PL spectra derived from different sample spots as characterized by PFM: the spectra were recorded at the same spot as the PFM image shown in Fig. 2h (**a**), Fig. 2i (**b**), Supplementary Fig. 2c (**c**), Supplementary Fig. 6b (**d**) and Supplementary Fig. 6c (**e**). **f–j**, Corresponding angular dependence of the PL emission (blue dots, with fits represented as blue curves). The degree of linear polarization (P) is given by $P = (I_{max} - I_{min})/(I_{max} + I_{min})$, where I_{max} (I_{min}) is the maximum (minimum) PL emission intensity. **k–o**, Corresponding angular distribution in the 2D FFTs of the PFM images (coloured fans). The golden and light-golden sectors represent the angular distributions of the primary oval structures in the strained moiré landscapes, the green sectors represent the angular distributions of the secondary pseudo-1D stripes formed by the primary structures and the blue double-headed arrows highlight the PL optical polarization directions determined in **f–j**. Excitation density $n_{ex} = 2.5 \times 10^{11}$ cm^{-2} (otherwise the same experimental conditions as in Fig. 1e).

The fitting results to the PL from multiple spots on the PL map are summarized in Supplementary Fig. 9. Importantly, the direction of linear polarization, which we correlate with the direction of the primary structure in 1D moiré strips, evolves from spot to spot, suggesting the spatial evolution of strain fields in the sample. On the other hand, the PL intensity is independent of the polarization of excitation light, at the intralayer exciton energy, as shown by the isotropic dependence (orange dots in Supplementary Fig. 9e). Thus, we infer that the 1D moiré pattern has a negligible effect on the intralayer excitons, for which the moiré potential is expected to be shallower than that for interlayer excitons[1]. The heterostrain field can vary locally depending on fabrication details and sample condition, such as the presence of bubbles in the heterobilayer or between the heterobilayer and the h-BN encapsulation layers. Both 0D and 1D moiré traps can coexist in different regions of the same sample. Supplementary Fig. 10 shows both type-I and type-II PL at different locations of a single WSe$_2$/MoSe$_2$ heterobilayer sample with $\Delta\theta = 2.6 \pm 0.5°$. By contrast to the linearly polarized type-II PL, the circularly polarized type-I PL in Supplementary Fig. 4 is close to isotropic in the azimuthal angle-resolved polarization distribution (Supplementary Fig. 11).

Note that the widths of type-II PL from fully h-BN encapsulated samples were FWHM $= 8 \pm 2$ meV (see the lower spectrum in Fig. 1e, the lower two spectra in Supplementary Fig. 9c, the four spectra from different spots in Supplementary Fig. 10e and the spectra obtained at low excitation densities in Fig. 1a in ref. [12]). For comparison, the PL peak width in the absence of the top h-BN excapsulation layer doubles to FWHM $= 16 \pm 4$ meV, but the asymmetric peak shape is retained, as shown in Fig. 3b,c. This broadening can be attributed to dielectric heterogeneity[23], resulting, for

example, from the adsorption of molecules on the WSe$_2$/MoSe$_2$ sample surface under cryogenic measurements. For some spots, the broadened PL peak can be attributed to the sum of two peaks, as in Fig. 3a,d,e. This likely results from the presence of two different dielectric environments or two domains of strained moiré patterns of ~1-µm diameter spots in the probe region.

The results presented above establish that the linearly polarized PL comes from excitons in the 1D potential of a strained moiré landscape, with the direction of the linear polarization determined by the direction of the primary 1D moiré pattern. We can qualitatively understand the linear exciton emission from the highly anisotropic electron–hole wave functions in the 1D moiré potential from the breaking of the C_3 rotational symmetry, which leads to the hybridization of the two valley configurations of excitons from the electron–hole exchange interaction[24–26], and from analogies with the known linear PL from quantum wires reported in previous studies[27,28]. We analysed the contrasting PL features of type-I and type-II emission at a qualitative level with a 2D harmonic trap model (Supplementary Text 2 and 3 and Supplementary Figs. 22–24). Because the process of forming interlayer excitons from higher-energy intralayer excitons is always accompanied by excess energy, which amounts to ~300 meV for the WSe$_2$/MoSe$_2$ heterobilayer[13,16,17], radiative recombination may occur from excitonic levels higher than the lowest-energy state. A 0D moiré potential hosts very few bound states and the lowest exciton state likely dominates PL emission, leading to quantum emitter-like sharp PL peaks. Compared with the 0D moiré trap, a 1D moiré trap is characterized by higher density of states with densely spaced excitonic levels (Supplementary Fig. 22c), and radiative recombination from multiple levels may occur, leading to both broadening of the PL
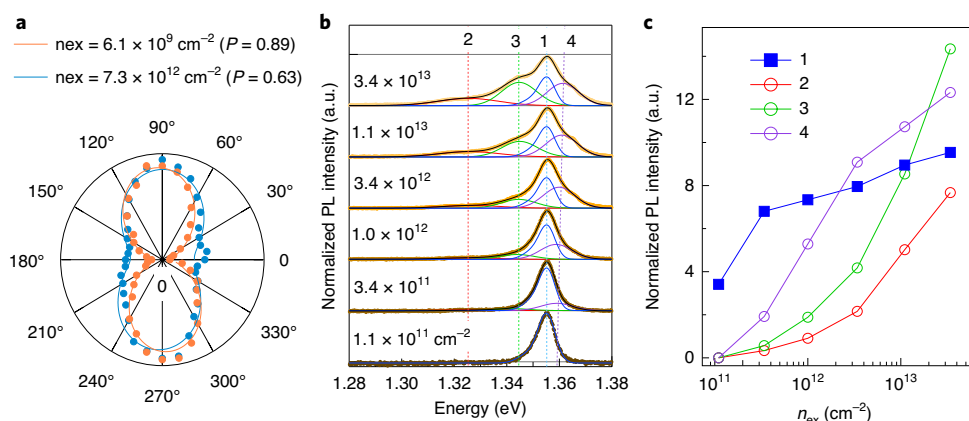
Fig. 4 | Evolution of PL peak shape with exciton density for interlayer excitons in the 1D moiré potential. The data were obtained on the same sample as used to collect the data presented in Fig. 2. **a**, Linear polarization distributions of the PL emission at two excitation densities. The coloured dots are data points and the solid curves are fits. **b**, PL spectra (orange lines) acquired with excitation densities varying from $n_{ex} = 1.1 \times 10^{11}$ to 3.4×10^{13} cm^{-2}. The coloured curves are deconvolutions as detailed in the text. The vertical dashed lines mark the peak positions (1–4) of the four deconvoluted peaks. **c**, Integrated intensities of the deconvoluted PL peaks 1–4 shown in **b** as a function of excitation density. Sample temperature = 4 K.

peak and an increase in the total PL intensity. To understand the linear polarization, we considered the anisotropic envelope function in the harmonic trap and electron–hole exchange interaction. As detailed in Supplementary Text 3 and Supplementary Figs. 23 and 24, the intervalley electron–hole exchange interaction and the resulting valley–orbital coupling split the nominally degenerate interlayer excitons into two levels. The resulting exciton eigenstates are coherent superpositions of those from two distinct valleys in momentum space. The lower level gives interlayer exciton emission polarization along the elongated (y) direction and the higher level along the contracted (x) direction (Supplementary Fig. 23b). When the relaxation rate between these two levels is comparable to that between the neighbouring eigen levels of the harmonic trap, the intensity of the PL emission from the lower level is much higher than that from the upper level (Supplementary Fig. 24d), resulting in predominantly linear polarization along the elongated (y) direction of the primary 1D moiré potential. Although the harmonic trap model presented above provides a tentative and qualitative interpretation of the experimental correlation between linear polarized PL and the direction of the primary 1D moiré potential, a quantitative theoretical treatment that takes into account local atomic registry and the symmetry of the strained 1D moiré landscape is a challenge. Such theoretical treatment was beyond the scope of this experimental study but deserves future theoretical efforts.

Escaping the moiré traps at high exciton densities
Because both 0D and 1D moiré potential traps are shallow in a 2D landscape, we expect interlayer excitons to also form outside these traps at sufficiently high excitation densities due to mutual repulsion between these excitons with permanent electric dipoles[1]. This is confirmed for the 1D moiré potential, as shown in Fig. 4. The first evidence comes from the reduction of linear polarization. Figure 4a shows that when the excitation density increases from 6.1×10^9 to 7.3×10^{12} cm^{-2}, the purity of the linear polarization, $P = (I_{max} - I_{min})/(I_{max} + I_{min})$, decreases from 0.89 to 0.63. The second evidence comes from the evolution of peak shapes. As shown in Fig. 4b, with increasing n_{ex}, the single PL peak attributed to the 1D moiré exciton evolves into a multipeak shape, with the growth of shoulder features on both the lower- and higher-energy sides. This evolution is particularly evident above the Mott density ($n_{Mott} \approx 3 \times 10^{12}$ cm^{-2})[13].

The solid curves in Fig. 4b show approximate deconvolutions of the spectra into the main asymmetric PL peak 1 and three Gaussian

peaks 2–4, with their positions shown by the dashed lines. Peaks 2 and 3 are on the lower-energy side of the main peak, and peak 4 is on the higher-energy side. Similarly, we observe the evolution of the initially quantum emitter-like type-I moiré excitons into broader multiple PL peak-shapes as the excitation density is increased above n_{Mott}, as shown in Supplementary Figs. 12 and 13. These results suggest radiative recombination from the increased population of interlayer excitons outside the 0D or 1D moiré traps at sufficiently high excitation density, as is demonstrated also for both type-I and type-II PL from the same sample (Supplementary Fig. 14). The exact origin of the multiple PL peak shapes for interlayer excitons in the WSe$_2$/MoSe$_2$ heterobilayer at high excitation densities is not well understood at present. A recent report[7] attributed similar multiple peaks in the WSe$_2$/MoSe$_2$ heterobilayer to quantized levels within the 0D moiré trap. Here, we observe the multiple PL peaks in most WSe$_2$/MoSe$_2$ heterobilayer samples only at high excitation densities, regardless of the initial nature of the moiré excitons (type-I or type-II). This suggests that the four-peak structure originates from radiative recombination of free interlayer excitons outside the moiré traps.

In both WSe$_2$/MoSe$_2$ and MoS$_2$/WS$_2$ heterobilayers, density functional theory calculations suggest that the conduction band minima are at the Q point, not the K point[29,30]. Thus, the two emission peaks on the lower-energy side of the main PL peak may be attributed to the spin–orbital split conduction bands at Q involving the momentum-indirect excitons Q$_C$–K$_V$, where the subscripts C and V denote the conduction and valence bands, respectively. Previous pump-probe reflectance and time-resolved PL measurements on WSe$_2$/MoSe$_2$ heterobilayers revealed efficient scattering from the K to Q valleys in the Brillouin zone[13]. In the related system of WS$_2$/MoS$_2$, a time- and angle-resolved photoemission spectroscopy (TR-ARPES) study provided direct evidence for photoexcited electrons in the Q valleys that have a strongly mixed character of both TMDC monolayers[31]. Similarly, the emission peak on the high-energy side may arise from momentum-indirect K*$_C$–K$_V$' involving the upper spin–orbital split conduction band (denoted *). Radiative emission from these momentum-indirect excitons can be facilitated at high density through pair annihilation with momentum conservation satisfied, as detailed in Supplementary Fig. 15. Similar to the proposed mechanism for the annihilation of bright excitons[32] (see Supplementary Fig. 12d in ref. [32]), a pair of intervalley dark excitons, K*$_C$–K$_V$' (blue arrow) and K*$_C$'–K$_V$ (blue dashed arrow), can virtually interchange the electron–hole pairing and thus

emit two photons through the intermediate state of two bright excitons (peak 4). Similarly, for a pair of dark Q_C–K_V and Q_C'–K_V' excitons, the pairwise Q to K and Q' to K' scattering of their electrons into two virtual K_C–K_V and K_C'–K_V' bright excitons can provide the radiative emission channel (peaks 2 and 3). Radiative recombination from the pair annihilation of dark excitons is expected at higher exciton density than the normal PL emission from the bright K_C–K_V exciton. Supporting this, we note that the multiple peaks (2–4) attributed to momentum-indirect excitons are vanishingly small at low excitation densities ($\leq 1 \times 10^{11}\,cm^{-2}$), but grow much faster with increasing n_{ex} than peak 1 (Fig. 4c).

Implications of strain in moiré physics

The discovery of the 1D moiré potential landscape from uniaxial strain and the corresponding excitons in TMDC heterobilayers has two implications in the growing field of moiré physics. On the one hand, given the susceptibility of 2D crystals to strain in samples consisting of multilayers created by mechanical transfer stacking, the presence of strain fields must be considered to understand the influence of the moiré potential and its heterogeneity on physical properties. On the other hand, its very sensitivity to strain field provides a new method to control the moiré potential landscape in heterobilayers, leading to optical and electronic responses on demand. The 1D moiré potential is particularly attractive for strongly correlated and anisotropic charge transport[4,33]. In comparison with the large strain required to bring about significant changes in monolayers of graphene[34–36] and TMDCs[37–39], moiré strain engineering can be achieved with a modest differential strain in the order of the lattice mismatch[4]. Combined with the twist angle, the active or passive control of strain fields thus opens the door to greater opportunities for artificially generating band structures[33] and topological mosaics[4] at 2D material interfaces.

Online content

Any methods, additional references, Nature Research reporting summaries, source data, extended data, supplementary information, acknowledgements, peer review information; details of author contributions and competing interests; and statements of data and code availability are available at https://doi.org/10.1038/s41563-020-0730-8.

References

1. Yao, W., Xu, X., Liu, G.-B., Tang, J. & Yu, H. Moiré excitons: from programmable quantum emitter arrays to spin–orbit–coupled artificial lattices. *Sci. Adv.* **3**, e1701696 (2017).
2. Cao, Y. et al. Unconventional superconductivity in magic-angle graphene superlattices. *Nature* **556**, 43–50 (2018).
3. Cao, Y. et al. Correlated insulator behaviour at half-filling in magic-angle graphene superlattices. *Nature* **556**, 80–84 (2018).
4. Tong, Q. et al. Topological mosaics in moiré superlattices of van der Waals heterobilayers. *Nat. Phys.* **13**, 356–362 (2017).
5. Fogler, M. M., Butov, L. V. & Novoselov, K. S. High-temperature superfluidity with indirect excitons in van der Waals heterostructures. *Nat. Commun.* **5**, 4555 (2014).
6. Seyler, K. L. et al. Signatures of moiré-trapped valley excitons in $MoSe_2$/WSe_2 heterobilayers. *Nature* **567**, 66–70 (2019).
7. Tran, K. et al. Evidence for moiré excitons in van der Waals heterostructures. *Nature* **567**, 71–75 (2019).
8. Yuan, L. et al. Twist-angle-dependent interlayer exciton diffusion in WS_2–WSe_2 heterobilayers. *Nat. Mater.* **19**, 617–623 (2020).
9. Li, W., Lu, X., Dubey, S., Devenica, L. & Srivastava, A. Dipolar interactions between localized interlayer excitons in van der Waals heterostructures. *Nat. Mater.* **19**, 624–629 (2020).
10. Brotons-Gisbert, M. et al. Spin–layer locking of interlayer excitons trapped in moiré potentials. *Nat. Mater.* **19**, 630–636 (2020).
11. Wu, F., Lovorn, T. & Macdonald, A. H. Topological exciton bands in moiré heterojunctions. *Phys. Rev. Lett.* **118**, 147401 (2017).
12. Wang, L. et al. One-dimensional electrical contact to a two-dimensional material. *Science* **342**, 614–617 (2013).
13. Wang, J. et al. Optical generation of high carrier densities in 2D semiconductor heterobilayers. *Sci. Adv.* **5**, eaax0145 (2019).
14. Rivera, P. et al. Interlayer valley excitons in heterobilayers of transition metal dichalcogenides. *Nat. Nanotechnol.* **13**, 1004–1015 (2018).
15. Li, Y. et al. Probing symmetry properties of few-layer MoS_2 and h-BN by optical second-harmonic generation. *Nano Lett.* **13**, 3329–3333 (2013).
16. Rivera, P. et al. Observation of long-lived interlayer excitons in monolayer $MoSe_2$–WSe_2 heterostructures. *Nat. Commun.* **6**, 6242 (2015).
17. Jauregui, L. A. et al. Electrical control of interlayer exciton dynamics in atomically thin heterostructures. *Science* **366**, 870–875 (2019).
18. Wu, W. et al. Piezoelectricity of single-atomic-layer MoS_2 for energy conversion and piezotronics. *Nature* **514**, 470–474 (2014).
19. Lee, J. H. et al. Reliable piezoelectricity in bilayer WSe_2 for piezoelectric nanogenerators. *Adv. Mater.* **29**, 1–7 (2017).
20. Mcgilly, L. J. et al. Visualization of moiré superlattices. *Nat. Nanotechnol.* (in the press).
21. Liu, G. et al. Electronic structures and theoretical modelling of two-dimensional group-VIB transition metal dichalcogenides. *Chem. Soc. Rev.* **44**, 2643–2663 (2014).
22. Ajayi, O. et al. Approaching the intrinsic photoluminescence linewidth in transition metal dichalcogenide monolayers. *2D Mater.* **4**, 31011 (2017).
23. Raja, A. et al. Dielectric disorder in two-dimensional materials. *Nat. Nanotechnol.* **14**, 832–837 (2019).
24. Yu, H., Liu, G.-B., Gong, P., Xu, X. & Yao, W. Dirac cones and Dirac saddle points of bright excitons in monolayer transition metal dichalcogenides. *Nat. Commun.* **5**, 3876 (2014).
25. Yu, T. & Wu, M. W. Valley depolarization due to intervalley and intravalley electron-hole exchange interactions in monolayer MoS_2. *Phys. Rev. B* **89**, 205303 (2014).
26. Glazov, M. M. et al. Exciton fine structure and spin decoherence in monolayers of transition metal dichalcogenides. *Phys. Rev. B* **89**, 201302 (2014).
27. Wang, J., Gudiksen, M. S., Duan, X., Cui, Y. & Lieber, C. M. Highly polarized photoluminescence and photodetection from single indium phosphide nanowires. *Science* **293**, 1455–1457 (2001).
28. Lefebvre, J., Fraser, J. M., Finnie, P. & Homma, Y. Photoluminescence from an individual single-walled carbon nanotube. *Phys. Rev. B* **69**, 75403 (2004).
29. Gillen, R. & Maultzsch, J. Interlayer excitons in $MoSe_2$/WSe_2 heterostructures from first principles. *Phys. Rev. B* **97**, 1–7 (2018).
30. Okada, M. et al. Direct and indirect interlayer excitons in a van der Waals heterostructure of $hBN/WS_2/MoS_2/hBN$. *ACS Nano* **12**, 2498–2505 (2018).
31. Liu, F., Li, Q. & Zhu, X. Direct determination of momentum-resolved electron transfer in the photoexcited van der Waals heterobilayer WS_2/MoS_2. *Phys. Rev. B* **101**, 201405(R) (2020).
32. Rivera, P. et al. Valley-polarized exciton dynamics in a 2D semiconductor heterostructure. *Science* **351**, 688–691 (2016).
33. Bi, Z., Yuan, N. F. Q. & Fu, L. Designing flat bands by strain. *Phys. Rev. B* **100**, 35448 (2019).
34. Ni, Z. H. et al. Uniaxial strain on graphene: Raman spectroscopy study and band-gap opening. *ACS Nano* **2**, 2301–2305 (2008).
35. Gui, G., Li, J & Zhong, J. Band structure engineering of graphene by strain: first-principles calculations. *Phys. Rev. B* **78**, 75435 (2008).
36. Guinea, F., Katsnelson, M. I. & Geim, A. K. Energy gaps, topological insulator state and zero-field quantum Hall effect in graphene by strain engineering. *Nat. Phys.* **6**, 30–33 (2009).
37. Castellanos-Gomez, A. et al. Local strain engineering in atomically thin MoS_2. *Nano Lett.* **13**, 5361–5366 (2013).
38. He, K., Poole, C., Mak, K. F. & Shan, J. Experimental demonstration of continuous electronic structure tuning via strain in atomically thin MoS_2. *Nano Lett.* **13**, 2931–2936 (2013).
39. Kou, L., Frauenheim, T. & Chen, C. Nanoscale multilayer transition-metal dichalcogenide heterostructures: band gap modulation by interfacial strain and spontaneous polarization. *J. Phys. Chem. Lett.* **4**, 1730–1736 (2013).

Methods

TMDC monolayers. Monolayers of WSe_2 and $MoSe_2$ were mechanically exfoliated from bulk crystals grown by the self-flux method. These monolayers possessed low defect densities ($<10^{11}$ cm^{-2})[40]. Flakes of h-BN with a thickness of 5–35 nm and atomically flat surfaces were obtained by mechanical exfoliation. The flakes (WSe_2, $MoSe_2$ and h-BN) were characterized by AFM and Raman spectroscopy.

Determination of TMDC zigzag crystal orientation by SHG. The crystal orientations of WSe_2 and $MoSe_2$ monolayers were determined by SHG measurements with an inverted optical microscope (Olympus IX73). Linearly polarized femtosecond laser light (Spectrum Physics Tsunami, 80 MHz, 800 nm, 80 fs) was focused onto a monolayer with a ×100, numerical aperture 0.80 objective (Olympus LMPLFLN100X). The reflected SHG signal at 400 nm was collected using the same objective, filtered through a short-pass dichroic mirror, short-pass and band-pass filters, and a Glan–Taylor linear polarizer, detected by a photomultiplier tube (Hamamatsu R4220P) and recorded with a photon counter (BK PRECISION 1823A 2.4 GHz Universal Frequency Counter). We obtained the azimuthal angular (θ) distribution of the SHG signal by rotating the laser polarization and the SHG signal (with a half-wave plate) with the sample in a fixed orientation. Due to the D_{3h} symmetry, the non-vanishing tensor elements of the second-order susceptibility ($\chi^{(2)}$) of the WSe_2 and $MoSe_2$ monolayers are given by $\chi^{(2)}_{yyy} = -\chi^{(2)}_{yxx} = -\chi^{(2)}_{xxy} = -\chi^{(2)}_{xyx}$, where the x axis is defined as the zigzag direction[15]. When we simultaneously rotated the fundamental and SHG signals, the SHG intensity showed six-fold symmetry: $I_\perp \propto \cos^2(3\theta)$ and $I_\parallel \propto \sin^2(3\theta)$, where θ is the angle between the laser polarization and the zigzag direction. We used triangular flakes of monolayer WS_2 (6Carbon) or MoS_2 (2DLayer), for which the zigzag directions are the same as the crystal edges, both grown by chemical vapour deposition (CVD), to calibrate the SHG setup.

Preparation of the 2D WSe_2/$MoSe_2$ heterostructure samples. The 2D WSe_2/$MoSe_2$ heterobilayer samples were prepared by the polymer-free van der Waals assembly technique[12]. A transparent polydimethylsiloxane (PDMS) stamp coated with a thin layer of polypropylene carbonate (PPC) was used to pick up a thin layer of exfoliated h-BN. This h-BN was then used to pick up the first TMDC monolayer. The second TMDC monolayer was aligned with and picked up by the first monolayer on a rotation stage. After picking up a second h-BN flake as the bottom encapsulation layer, we transferred the entire structure onto a clean silicon wafer (with a 285-nm thermal oxide layer for enhanced optical contrast) at elevated temperatures (90–130 °C). The residual PPC was washed away with acetone to give a clean h-BN/WSe_2/$MoSe_2$/h-BN heterobilayer on the Si/SiO$_2$ substrate. The samples were then thermally annealed in an ultrahigh vacuum chamber (10^{-8}–10^{-9} torr). The sample temperature was raised from room temperature to 523 K slowly over 2 h and kept at this temperature (523 K) for 3 h. Then, the sample was cooled to 173 K over 30 min, after which the temperature of the sample was slowly increased to room temperature over 12 h.

Polarization-resolved confocal microscopic measurements. PL imaging was performed on a home-built scanning confocal microscope system (Supplementary Fig. 16) based on a liquid helium recirculating optical cryostat (Montana Instruments Fusion/X-Plane) with a ×100, numerical aperture 0.75 objective (Zeiss LD EC Epiplan-Neofluar ×100/0.75 HD DIC M27). The temperature of the sample stage could be varied between 3.8 and 350 K. In all the experiments presented in this study, the TMDC heterobilayer and monolayers samples were maintained at 4 K in a vacuum ($<10^{-6}$ torr) environment unless otherwise noted. A Galvo-Galvo scanner (Thorlabs) was used for mapping the PL signal emitted from the sample plane. Polarizers and $\lambda/2$ and $\lambda/4$ waveplates were used for the circular/linear polarization-resolved experiments (see Supplementary Fig. 16 for the detailed optical setup). The incident laser beam (Coherent Rega, 750 nm, ~150 fs, 76 MHz) was focused by the objective to a diffraction-limited spot on the sample. The excitation power was measured using a calibrated power meter (Ophir StarLite) with a broad dynamic range. The PL light was collected by the same objective, spatially and spectrally filtered, dispersed by a grating and detected using an InGaAs photodiode array (Princeton Instruments, PyLoN-IR). The wavelength was calibrated by neon–argon and mercury atomic emission sources (Princeton Instruments, IntelliCal). In all PL measurements, we found no laser heating of the sample under cryogenic cooling. The PL spectra were completely reproducible following repeated measurements at the same spot on each sample (for example, see Supplementary Fig. 17).

Piezoresponse force microscopy measurements. All PFM imaging experiments were performed on a commercially available Bruker Dimension Icon AFM with a Nanoscope IIIa controller. We used ASYELEC-01 Ti/Ir-coated silicon probes with a force constant of ~3 N m^{-1} from Oxford Instruments Asylum Research. The amplitudes of a.c. bias were <1 V, and the single frequency excitation was at the lateral cantilever-sample resonance in the range 750–850 kHz. Most PFM imaging experiments were carried out on WSe_2/$MoSe_2$ heterobilayer samples without the top h-BN encapsulation layer, with the sample stack either on PPC/PDMS or transferred onto SiO$_2$/Si. Similar PFM images were also obtained for WSe_2/$MoSe_2$ heterobilayer samples with thin h-BN capping layers (Supplementary Fig. 5), albeit at reduced resolution as compared with the exposed WSe_2/$MoSe_2$ heterobilayers. To eliminate the possibility of tip artefacts, we confirmed that the PFM images were reproducible by scanning in orthogonal directions. Note that the thermal annealing procedure used on some of the heterobilayer samples did not result in changes to the PFM images for either 0D or 1D moiré patterns (Supplementary Fig. 18).

Data availability
The data represented in Figs. 1–4 are provided with the article source data. All data that support the results in this article are available from the corresponding author upon reasonable request. Source data are provided with this paper.

References
40. Edelberg, D. et al. Approaching the intrinsic limit in transition metal diselenides via point defect control. *Nano Lett.* **19**, 4371–4379 (2019).

Author contributions
X.Y.Z., Y.B. and L.Z. conceived this work. Y.B., L.Z., J.W. and W.W. performed the experiments. L.M., J.A., F.L., P.R. and N.R.F. participated in various stages of sample preparation and characterization. D.H. and C.F.B.L. carried out strain field analysis, with supervision from D.N.B. X.C.Y. and W.Y. carried out model Hamiltonian analysis. X.Y.Z. supervised the project, with inputs from A.P., J.H. and X.X. X.Y.Z, W.Y., X.X., J.H. and A.P. participated in the interpretation of experimental findings. X.Y.Z. and Y.B. wrote the manuscript, with inputs from all coauthors. All authors read and commented on the manuscript.

Competing interests
All authors declare no competing interests.

Additional information
Supplementary information is available for this paper at https://doi.org/10.1038/s41563-020-0730-8.

Correspondence and requests for materials should be addressed to A.N.P. or X.-Y.Z.

Reprints and permissions information is available at www.nature.com/reprints.